Li₇La₃Zr₂O₁₂ Interface Modification for Li Dendrite Prevention

Chih-Long Tsai,*[†,‡] Vladimir Roddatis,[§] C. Vinod Chandran,[‖] Qianli Ma,[†,‡] Sven Uhlenbruck,[†,‡] Martin Bram,[†,‡] Paul Heitjans,[‖] and Olivier Guillon[†,‡,⊥]

[†]Institute of Energy and Climate Research, Materials Synthesis and Processing (IEK-1), Forschungszentrum Jülich GmbH, 52425 Jülich, Germany

[‡]Jülich Aachen Research Alliance: JARA-Energy

[§]Institute of Materials Physics, University of Göttingen, Friedrich-Hund-Platz 1, 37077 Göttingen, Germany

[‖]Institute of Physical Chemistry and Electrochemistry, Leibniz University Hannover, Callinstrasse 3-3a, 30167 Hannover, Germany

[⊥]Institute of Mineral Engineering, Rheinisch-Westfälische Technische Hochschule (RWTH) Aachen University, Mauerstrasse 5, 52064 Aachen, Germany

S *Supporting Information*

ABSTRACT: Al-contaminated Ta-substituted $Li_7La_3Zr_2O_{12}$ (LLZ:Ta), synthesized via solid-state reaction, and Al-free Ta-substituted $Li_7La_3Zr_2O_{12}$, fabricated by hot-press sintering (HP-LLZ:Ta), have relative densities of 92.7% and 99.0%, respectively. Impedance spectra show the total conductivity of LLZ:Ta to be 0.71 mS cm^{-1} at 30 °C and that of HP-LLZ:Ta to be 1.18 mS cm^{-1}. The lower total conductivity for LLZ:Ta than HP-LLZ:Ta was attributed to the higher grain boundary resistance and lower relative density of LLZ:Ta, as confirmed by their microstructures. Constant direct current measurements of HP-LLZ:Ta with a current density of 0.5 mA cm^{-2} suggest that the short circuit formation was neither due to the low relative density of the samples nor the reduction of Li−Al glassy phase at grain boundaries. TEM, EELS, and MAS NMR were used to prove that the short circuit was from Li dendrite formation inside HP-LLZ:Ta, which took place along the grain boundaries. The Li dendrite formation was found to be mostly due to the inhomogeneous contact between LLZ solid electrolyte and Li electrodes. By flatting the surface of the LLZ:Ta pellets and using thin layers of Au buffer to improve the contact between LLZ:Ta and Li electrodes, the interface resistance could be dramatically reduced, which results in short-circuit-free cells when running a current density of 0.5 mA cm^{-2} through the pellets. Temperature-dependent stepped current density galvanostatic cyclings were also carried out to determine the critical current densities for the short circuit formation. The short circuit that still occurred at higher current density is due to the inhomogeneous dissolution and deposition of metallic Li at the interfaces of Li electrodes and LLZ solid electrolyte when cycling the cell at large current densities.

KEYWORDS: $Li_7La_3Zr_2O_{12}$, LLZ, Li ion conductivity, dendrite, solid electrolyte
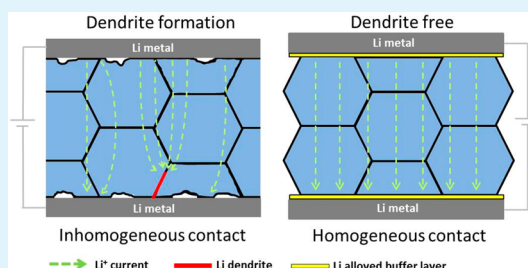
INTRODUCTION

The application of metallic Li as anode for rechargeable Li batteries is the ultimate dream due to its low native electrochemical potential (−3.04 V vs H₂), extremely high specific capacity (3861 mA h g^{-1}), and low density (0.53 g cm^{-3} at room temperature). However, the use of metallic Li in a room-temperature rechargeable battery is not yet fully successful due to the difficulty of suppressing Li dendrite. Theoretical calculations using linear elasticity theory by Monroe and Newman suggest that Li dendrite can be prevented if the shear modulus of the used solid electrolyte or separator is more than twice that of metallic Li, ~3.4 GPa.[1] Moreover, Brissot et al. concluded that the time for Li dendrite starting to grow, i.e. Sand's time, approaches infinity if the used electrolyte has a Li ion transfer number close to 1.[2] In other words, the dendrite growth would theoretically stop when a pure Li ion conductor is used as electrolyte in a Li battery. Accordingly, the two requirements make garnet-structured

$Li_7La_3Zr_2O_{12}$ (LLZ) solid-state Li ion conductor an ideal material for use as an electrolyte in rechargeable Li batteries because of its Li ion transfer number of unity, high mechanical strength, high shear modulus of ~55 GPa, and chemical stability against metallic Li.[3−6]

However, Li dendrite formation was reported by Ishiguro et al.[7,8] for their Nb- and Ta-substituted LLZ and Sudo et al.,[9] Suzuki et al.,[10] and Cheng et al.[11] for their Al-substituted LLZ. When a constant direct current (dc) was applied to a LLZ using Li as electrodes, i.e. with a cell structure of Li/LLZ/Li, the cells either show a stable performance at a current density ≤100 μA cm^{-2} or a short circuit formation at a current density of 0.5 mA cm^{-2}.[7−10] As reported by Ishiguro et al.,[7] only a setup of Li/Nb-substituted LLZ/In was stable for 4000 s under a current

density of 0.5 mA cm^{-2}. Later, Suzuki et al. showed that a short-circuit-free cell was achieved by using a transparent cubic-structured Al$_2$O$_3$-doped LLZ, which was produced by hot isostatic pressing.[10] Conclusions from refs 7−10 are that the formation of a short circuit has no clear dependence on the relative density of LLZ and that the lithium ion diffusion kinetics at grain boundaries is the key factor for the short circuit formation, for which the lower the grain boundary conductivity, the longer the cell is short-circuit-free. Efforts were also carried out by Sudo et al. to identify the reason for the short circuit, and they suggested that the Li dendrite may be the explanation.[9]

On the other hand, Cheng et al. reported that smaller grain sizes of Al-substituted LLZ, about 20−40 μm instead of 100−200 μm in diameter, greatly improved the constant current density cycle performances due to its lower interfacial resistance.[11] They concluded that the better performance observed from small-grained samples was attributed to the larger relative amount of higher conductive grain boundaries than grains, which is in conflict with the observation from refs 7−10. Cheng et al. reference the better conducting behavior of grain boundary than grain in Al-substituted LLZ above −10 °C to the work of Tenhaeff et al.[12] and not to their own measurement. Generally, the model of impedance results is based on a brick layer model that envisions the microstructure as an array of cubic grains and allows for intra- and intergranular conduction. A specific (true) conductivity that takes into account the thickness of the grain boundary should be considered when discussing the ion conducting path inside a polycrystalline material to avoid the affect from microstructure differences.[13] By applying the model, when a grain boundary arc is observed in the Nyquist plot, which was observed in the report of Tenhaeff et al. up to the highest temperature at 60 °C,[12] the true grain boundary conductivity must be much smaller than that of the grain interiors, since grain boundaries are usually much smaller than grains. Accordingly, the claim of better conductivity along the grain boundary than the grain could be improper for Cheng et al.[11] and makes the conclusion unsettled. On the other hand, the pointing out of inhomogeneous Li deposition and dissolution due to different conductivities along the grain and grain boundary by Cheng et al. brought the impetus to modify the interface to minimize the conductivity effect, which accelerates the realization of using metallic Li as an anode for all solid-state Li batteries.

In this work, efforts are made to answer the following questions that rise from refs 7−11:

(1) Are the relative densities of the materials high enough to provide pinhole-free pellets? Even though the reported relative densities for the tested samples were all higher than 92% and the hot isostatic pressed Al$_2$O$_3$-doped LLZ had a relative density as high as 99.1%, no clean and large-area microstructures of the prepared samples were shown in the reports.

(2) The times to form short circuits under the high current density, i.e., 0.5 mA cm^{-2}, were all within a couple hundreds of seconds, which is relatively short. Could the short circuit be formed by reducing materials along grain boundary instead of depositing metallic Li through the pellet? Especially, the reported materials were all contaminated by Al$_2$O$_3$ during the sintering processes due to the use of alumina crucibles. Eichinger reported that all Li−Al−O compounds other than Li$_5$AlO$_4$ can be reduced to Li−Al alloy when against molten lithium.[14]

(3) The starting voltages for constant dc measurements were all much higher than the calculated voltage when alternating current (ac) total conductivities of the materials are used for calculating the theoretical voltage across the cells without taking into account contact resistances, i.e.

$$V = \frac{Id}{\sigma A} \tag{1}$$

where I is the applied current, d is the sample thickness, σ is the ac total conductivity of the used solid electrolyte, and A is the sample area. The high overpotential, or contact resistance between the electrolyte and electrodes, implies that the used electrodes, i.e., metallic Li, were not properly attached to LLZ, even though efforts were also made to improve it. It is possible that the high interface resistance was formed by the inhomogeneous contacts between solid electrolyte and electrodes, which were later subjected to high effective current density. Li dendrite would, therefore, grow nearby these "point contacts" which actually undergo ultrahigh current density.

■ EXPERIMENTAL SECTION

Al-contaminated Ta-substituted LLZ (LLZ:Ta), i.e., Li$_{6.6}$La$_3$Zr$_{1.6}$Ta$_{0.4}$O$_{12}$, powder was prepared via a four steps solid-state reaction. The starting materials LiOH (Merck, 98%), La$_2$O$_3$ (Merck, 99.9%, predry at 900 °C for 10 h), ZrO$_2$ (Treibacher, 99.5%), and Ta$_2$O$_5$ (Inframat, 99.95%) were mixed in stoichiometric amounts with 20 mol % LiOH in excess. An extra 2.5 mol % of α-Al$_2$O$_3$ (Inframat, 99.9%) was added into the powder as a sintering additive. A motor grinder (Retsch RM 200) with a tungsten carbide crucible and pestle was used for dry mixing the prepared powder for 1 h with a rotational speed of 100 rpm. Then, the powder was pressed into pellets for 20 h sessions of calcination, once at 850 °C and twice at 1000 °C. Grinding and pressing were repeated between the calcination steps. The final calcined powder was ground into powder again for the sintering process. The total amount of the prepared powder was 500 g, so that the effect of powder quality on experimental results would be minimal. For Al-free Ta-substituted Li$_7$La$_3$Zr$_2$O$_{12}$, the preparation processes were all the same as described above without the additional α-Al$_2$O$_3$. In order to avoid any possible aluminum contamination from the environment, a graphite crucible and lid were used for the calcination steps under Ar atmosphere in a molybdenum chamber furnace. The powder-processing procedures and calcination steps were the same as those for LLZ:Ta.

The hot-pressed Al-free Ta-substituted Li$_7$La$_3$Zr$_2$O$_{12}$ (HP-LLZ:Ta) was made with a FCT HP W 100 system. Densification experiments started by dry-pressing the calcined Al-free Ta-substituted Li$_7$La$_3$Zr$_2$O$_{12}$ powders using a uniaxial pressing machine (Paul-Otto Weber) and a self-made ϕ = 15 mm graphite die under a pressure of 15 MPa. The hot-pressing was conducted at 1150 °C under an Ar atmosphere and a pressure of 50 MPa for 2 h. The heating rate was 5 K min^{-1} and the samples freely cooled to room temperature. For LLZ:Ta, the sintering process and material handling followed the previously reported literature method[15] but with only 4 h dwell time at 1150 °C. Sintered pellets were sliced into ~0.65 mm thick slices by using a diamond saw and 100% ethanol for rinsing during the cutting.

The samples were characterized for their phase purity and structure using X-ray diffraction (XRD). For this purpose, a Bruker D 4 Endeavor device using Cu Kα radiation equipped with a 1D detector LYNXEY and a DIFFRAC^{plus} BASIC package released in 2009 was used. The relative densities of the samples were determined by the Archimedes method using water as the liquid media. The theoretical density, 5.35 g cm^{-3}, for calculating the relative density was derived from the XRD refinement result of LLZ:Ta. For microstructural investigations, samples were mirror-polished by SiC sandpapers up to 4000 grit and thermally etched at 1100 °C for 20 min in air. Images of the microstructure were taken by using a scanning electron microscopy (SEM) (TM 3000 tabletop microscope, Hitachi). Inductively coupled

plasma optical emission spectroscopy (ICP-OES) (Thermo Elemental, IRIS Intrepid) was used to determine the stoichiometry of the sintered HP-LLZ:Ta; 50 mg of the HP-LLZ:Ta was dissolved in a solution of 2 g of ammonium sulfate/4 mL H_2SO_4 with heat until the powder was complete dissolved. Then, the solution was diluted to 50 mL by using pure water for the ICP-OES analysis. The error bar for the ICP-OES is ±3% of the detected concentration when the concentration is >1%; otherwise, it is ±10%.

Electrochemical ac impedance spectra (IS) were recorded to characterize the samples' conductivity in the temperature range between −30 and 100 °C with intervals of 10 °C. For the measurements, a BioLogic VMP-300 multipotentiostat, combined with a climate chamber (Vötsch Industrietechnik VT 4002EMC), was used. Au was sputtered onto the LLZ:Ta and HP-LLZ:Ta as the blocking electrodes. In order to avoid the influence of moisture during the measurements, samples were installed inside Swagelok cells in an Ar-filled glovebox. The measured frequency was varied from 7 MHz to 1 Hz with an electrical field perturbation of 20 mV mm^{-1}. For each temperature, 2 h of dwell time was used for the system to reach thermal equilibrium before measurements were started. The obtained data were analyzed by Zview software.

Constant dc measurements and galvanostatic cyclings (GC) were also performed by using the BioLogic VMP-300 multipotentiostat. Typical dimensions of the tested pellets were ∼0.65 mm in thickness and 11.35 mm in diameter. Pellets were also mirror-polished by SiC sandpapers up to 4000 grit to ensure that their surfaces were flat before using. For the samples with Au buffer layers, thin layers of Au (∼20 nm) were sputtered onto both sides of the pellets by using a sputter coater (Cressington 108cuto coater) for a sputtering time of 20 s with a distance of 6.5 cm between the sample and a ϕ = 5.1 cm Au target. The sputtered current was 20 mA under an Ar pressure of ∼0.02 mbar. To determine the thickness of the sputtered Au layer, a prolonged deposition of 180 s was carried out. The thickness of the film was measured by SEM by extrapolating from the film thickness with 20 s of deposition time. The tested cells were prepared by sandwiching lithium metal foils (∼150 μm) as electrodes and Ni plates (∼0.5 mm) as current collectors in Swagelok cells in an Ar-filled glovebox. The surfaces of the used lithium foils were thoroughly scratched clean to obtain flashed surfaces by using a stainless steel blade. The pressure needed to maintain the contact of the tested cell inside a Swagelok cell was created by using a spring with a spring constant of 20 N cm^{-1}. The estimated pressure in all the tested cells was about 10 N cm^{-2}, which corresponded to a pressure of ∼0.1 MPa. Cells were heated up in a climate chamber to 100 °C to improve the contact between the LLZ and lithium foils for at least 5 h before use. The stepped current density GC was performed by applying a current for 30 min and then a 10 min open circuit voltage (OCV) before changing to the opposing current direction. The step width for changing current density was 100 μA cm^{-2}. The constant current GC was performed by applying a constant current for 2 h which followed by a 10 min OCV before switching to the opposing current direction. For the used Ar-filled glovebox, the purity levels of O_2, N_2, and H_2O were all <1 ppm.

For solid-state nuclear magnetic resonance (NMR), high-resolution transmission electron microscopy (HR-TEM), and electron energy loss spectroscopy (EELS) studies, samples of HP-LLZ:Ta prepared in the same way as for the constant dc measurements, however without Au buffer layers, were used. A constant current density of 0.5 mA cm^{-2} was applied to the samples continuously for 100 h so that the dendrite could intensively grow inside the samples. Then, the samples were polished with SiC sandpaper inside an Ar-filled glovebox to ensure that no metallic lithium resided on the surface of the pellets after the lithium foils were removed. Pristine HP-LLZ:Ta samples were also prepared for comparison with all the experiments.

HR-TEM and EELS were carried out by using a FEI Titan 80-300 environmental transmission electron microscope operated at 300 kV and equipped with a Gatan Quantum ER image filter. Samples were prepared by mechanical polishing followed by ion milling in a Gatan PIPS 691.

For NMR studies, two samples, namely, with and without short-circuit-inducing pellets, were powdered and packed in 2.5 mm rotors inside an Ar-filled glovebox. ^{7}Li magic-angle spinning (MAS) NMR spectra at 20 and 25 kHz of spinning speed were recorded with a Bruker 600 AV-III spectrometer operating at a ^{7}Li Larmor frequency of 233.3 MHz. The spectra were referenced against the ^{7}Li signal of a dilute LiCl solution. The optimized recycle delay used was 2 s. The radio frequency strength was approximately 50 kHz. Since the central transition signals of the quadrupolar nucleus ^{7}Li may have different nutation frequencies, a very small (π/20) pulse was employed for quantitative analysis of the single pulse sequence.

■ RESULTS AND DISCUSSION

The XRD patterns of LLZ:Ta and HP-LLZ:Ta which sintered at 1150 °C are shown in Figure S1 of the Support Information (SI). All XRD patterns were assigned to the garnet-type cubic structure $Li_7La_3Zr_2O_{12}$ with a space group of $Ia3d$, which was calculated from the result of Awaka et al.[16] No impurity phase was detected under the detective limitation of the used X-ray diffractometer.

The microstructures of LLZ:Ta and HP-LLZ:Ta are shown in Figure 1. The grain size varies from ∼6 to ∼30 μm in
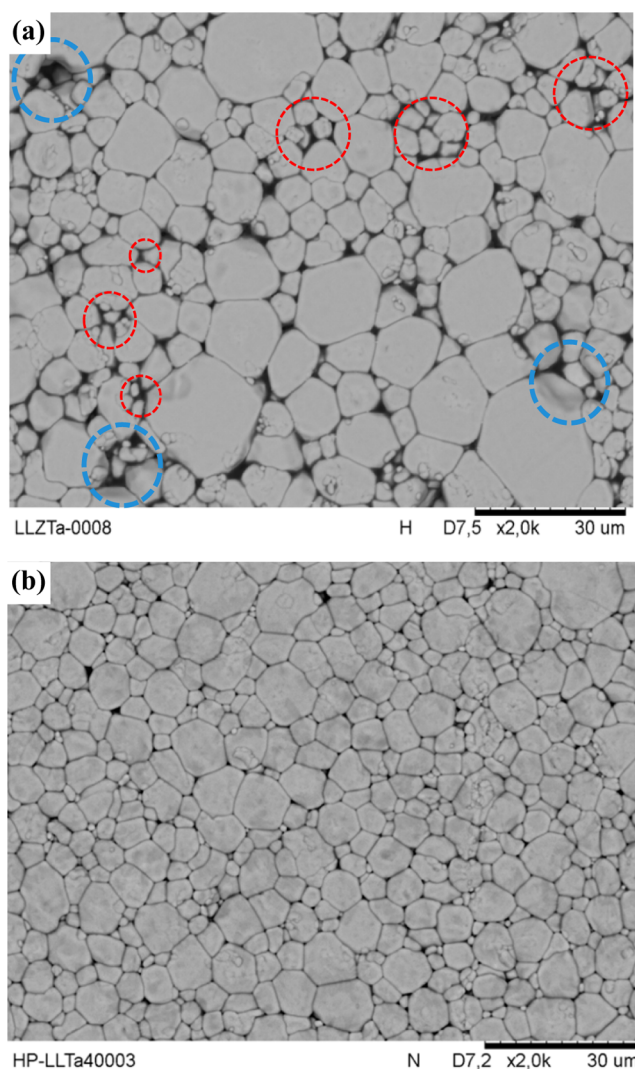

Figure 1. Microstructure of (a) LLZ:Ta and (b) HP-LLZ:Ta. The blue dashed circles indicate the closed porosity and red dashed circles indicate the Al−Li glassy phase between the grains.

diameter, as can be seen for LLZ:Ta (Figure 1a). Some closed pores, as indexed by blue dashed circles, were observed since the relative density of LLZ:Ta was only 92.7% (closed porosity 6.86%). A molten glassy Li−Al-rich phase that decorates between most of the grains can also be clearly seen, as indexed by red dashed circles, and is the residual material from the using of excess 20 mol % LiOH and intentionally added 2.5 mol % Al_2O_3. This Li−Al glassy phase is often found in Al-contaminated LLZ and is believed to serve as a sintering additive that helps the densification of the pellets during the sintering process, as reported by Kotobuki et al. and Kim et al.[17,18] During the sintering process of LLZ:Ta, an alumina crucible and lid were used. The lid was usually sealed to the crucible by lithium alumina, which is the product of Li vapor and the alumina crucible at high temperature and keeps the lithium partial pressure inside the crucible constant. The Li−Al glassy phase was kept inside the alumina crucible and decorated in between the grains. If the sintering process was conducted without the protection of a closed environment, decomposition of the garnet-structured LLZ:Ta to pyrochlore-phase $La_2Zr_2O_7$ can be found on the surface of the pellets, which is mostly due to the loss of Li at high temperature. On the other hand, the microstructure of HP-LLZ:Ta is more compact, with smaller grain sizes from ∼3 to 10 μm in diameter, than that of LLZ:Ta. Only a few small pores can be seen in between the grains, which is in agreement with the high relative density of 99.0% as measured by the Archimedes' method. Unlike LLZ:Ta, HP-LLZ:Ta shows clean grain boundaries without any impurity phase decorating in between the grains. The result from ICP-OES shows that no Al was detectable within the limitation of the machine. By normalizing the data to Zr concentration, ICP-OES gives a stoichiometry of $Li_{6.64}La_{2.99}Zr_{1.6}Ta_{0.41}O_{12.03}$ for HP-LLZ:Ta, which is very close to what was targeted at the powder preparation (Table S1, SI).

The Arrhenius plot of total conductivities for HP-LLZ:Ta and LLZ:Ta is shown in Figure 2a. In the Nyquist plots (Figure 2b), the contribution from grain boundary was only observable for LLZ:Ta at low temperatures, as a small deformation of the spectrum at frequency slightly above 4.2 kHz at −30 °C, but was not observed for HP-LLZ:Ta. This result agrees with the observation from microstructure studies that the grain boundaries of LLZ:Ta are much thicker than those of HP-LLZ:Ta due to the residual Li−Al glassy phase. Upon heating, no semicircle can be observed at temperatures higher than 20 °C for HP-LLZ:Ta and 40 °C for LLZ:Ta due to the frequency limitation of the used system. Since the contribution from grain boundary resistance to the total resistance was small, the separation of the small semicircle from the grain boundary to the grain was difficult and the grain boundary semicircle was only observable for a few points at low temperatures; only the total conductivities of LLZ:Ta and HP-LLZ:Ta are shown in the Arrheniuns plot (Figure 2a). HP-LLZ:Ta shows a higher total conductivity over the measured temperature range than LLZ:Ta. The difference between the total conductivities at the low-temperature range is larger than that at the high-temperature range due to the higher resistance contribution from the grain boundaries of LLZ:Ta. This agrees with the report by Tenhaeff et al. that the resistivity contribution from the grain boundary decreases faster than that of the grain interior when the temperature increases.[12] The total conductivity at 30 °C for HP-LLZ:Ta was 1.18 mS cm^{-1} and that for LLZ:Ta was 0.71 mS cm^{-1}, which are similar to or slightly higher than the values for other reported Ta-substituted

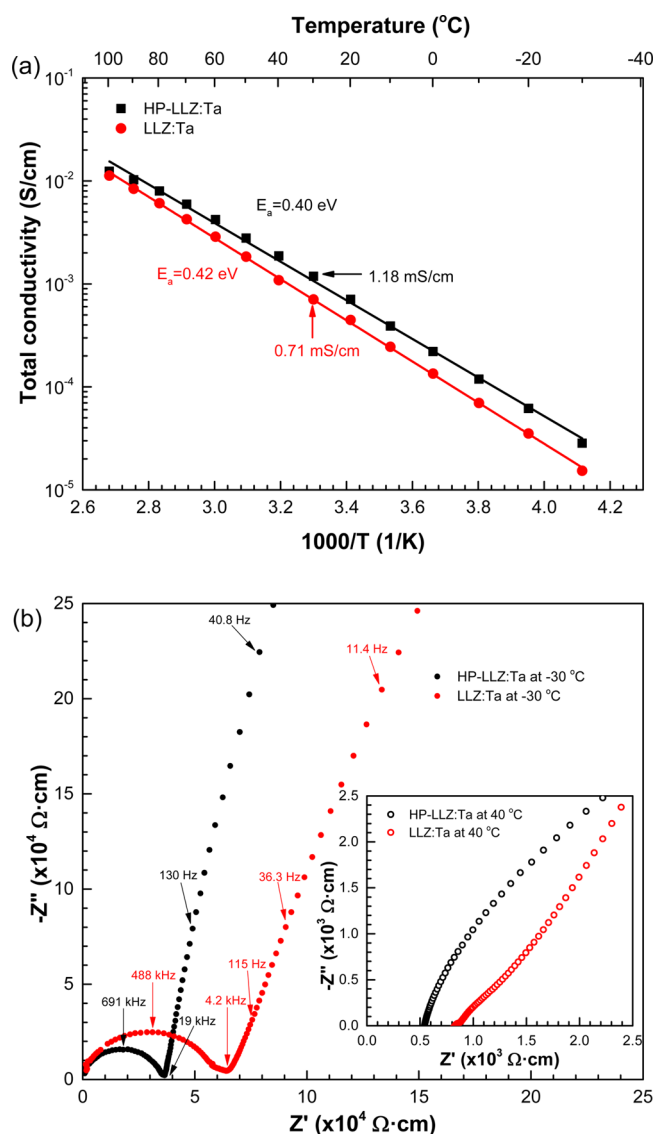**Figure 2.** (a) Arrhenius plot of total conductivity for LLZ:Ta and HP-LLZ:Ta and (b) the Nyquist plots for LLZ:Ta and HP-LLZ:Ta at −30 and 40 °C (inset). For the sake of readability σ_{total} vs $1000/T$ is shown. The activation energies given in the figure and text were calculated from fitting with eq 2.

LLZ.[19−25] From the fittings of the Arrhenius plots using the Arrhenius equation

$$\sigma T = A \exp\left(\frac{-E_a}{k_b T}\right) \quad (2)$$

where A is the pre-exponential factor, k_b is the Boltzmann constant, and T is the absolute temperature of the sample, the calculated activation energy E_a for HP-LLZ:Ta is 0.40 eV and that for LLZ:Ta is 0.42 eV. The slightly higher activation energy for LLZ:Ta than HP-LLZ:Ta is also attributed to the grain boundary, which has a higher activation energy than the grain.[12]

In order to answer the aforementioned questions in the Introduction, constant dc measurements with a current density of 0.5 mA cm^{-2} at 50 °C for Li/LLZ:Ta/Li and Li/HP-LLZ:Ta/Li cells were conducted. The experimental results are shown in Figure S2 (SI). Both of the pellets showed a short
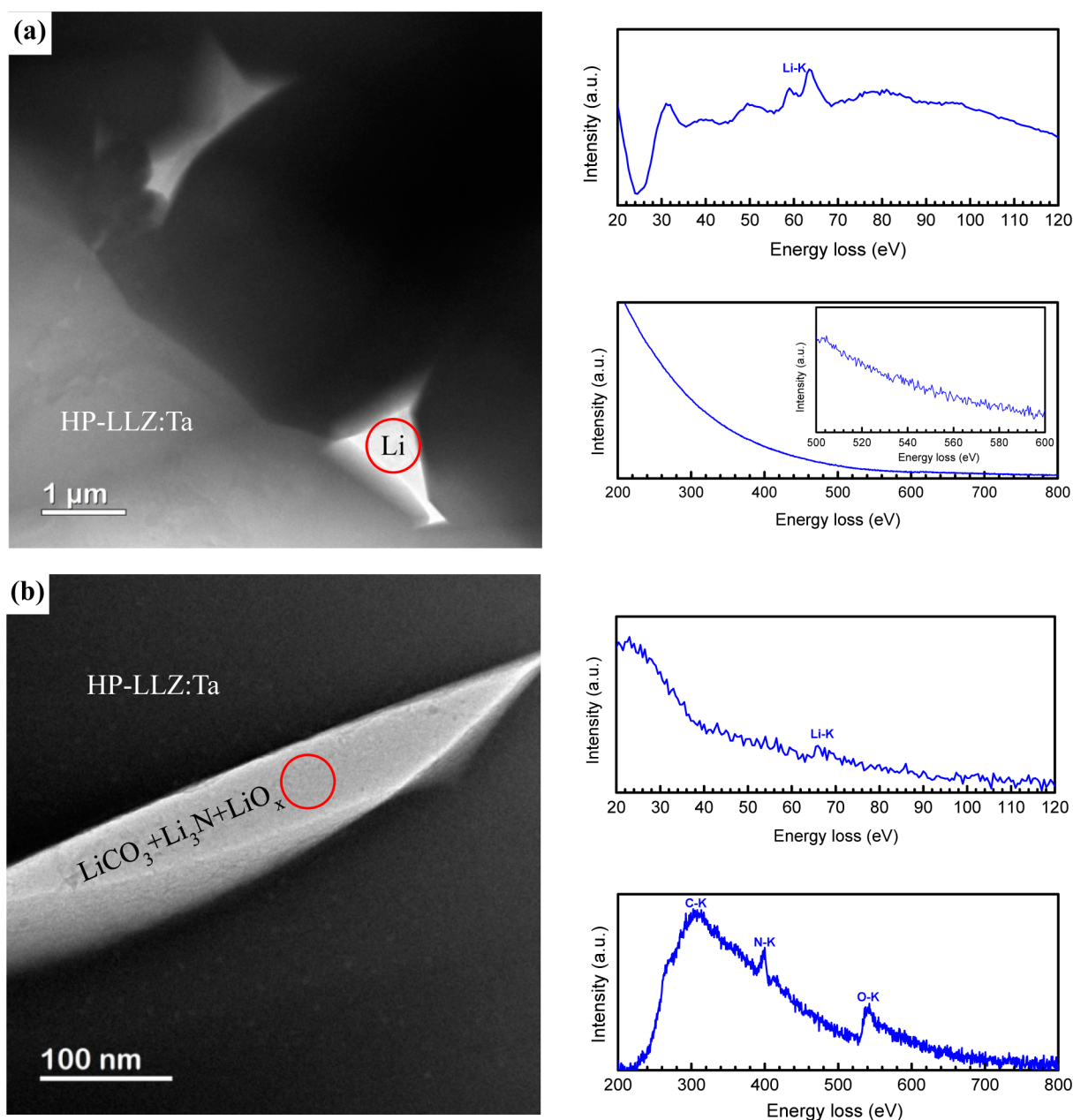
Figure 3. (Left) HR-TEM images and (right) EELS of HP-LLZ:Ta, where (a) only metallic Li and (b) Li_3N, Li_2CO_3, and LiO_x were found along the grain boundaries. The area used for the EELS is marked with the red circle.

circuit within 160 s. From the results, one can conclude that the formation of a short circuit is related to neither their relative density nor the possible pinholes across the pellet, since the HP-LLZ has a relative density as high as 99.0%, which is in agreement with previous observations.[7−10] The formation of a short circuit for the Li/HP-LLZ:Ta/Li cell indicates that reducing the Li−Al−O glassy compounds on the grain boundary into Li−Al metal alloy is not be the only reason for the short circuit formation. One thing to notice is that the starting voltages were much higher than their calculated voltages when the ac total conductivities were used without taking into account the contact resistance, i.e., 17.7 and 11.7 mV for Li/LLZ:Ta/Li and Li/HP-LLZ:Ta/Li cells, respectively. The high polarization voltage implies that the contacts between electrolyte and electrodes were not established properly, even though an effort was conducted to ensure the Li foils used were

properly attached. A similar phenomenon was also reported in refs 7−10, where an isostatic pressure of 150 MPa was used to ensure good contact between the Li foils and LLZ. When the short circuit was formed, the measured voltage stayed at ∼10 mV.

To understand what actually causes the short circuit, HR-TEM and EELS were used to reveal the possible reason. One can see in Figures 3 and S3 (SI) that the boundaries between adjacent HP-LLZ:Ta grains are still decorated with voids of different sizes. The EELS show that these voids are usually filled with Li oxide, which is the result of using 20 mol % more of LiOH in the precursor powder (Figure S3, SI). For Li oxide, one would expect that a voltage of more than 3 V is needed before Li oxide can be reduced into metallic Li, as in a Li−air battery.[26] Nevertheless, after careful searches on the sample, Li metal was found in some voids, which was confirmed by the
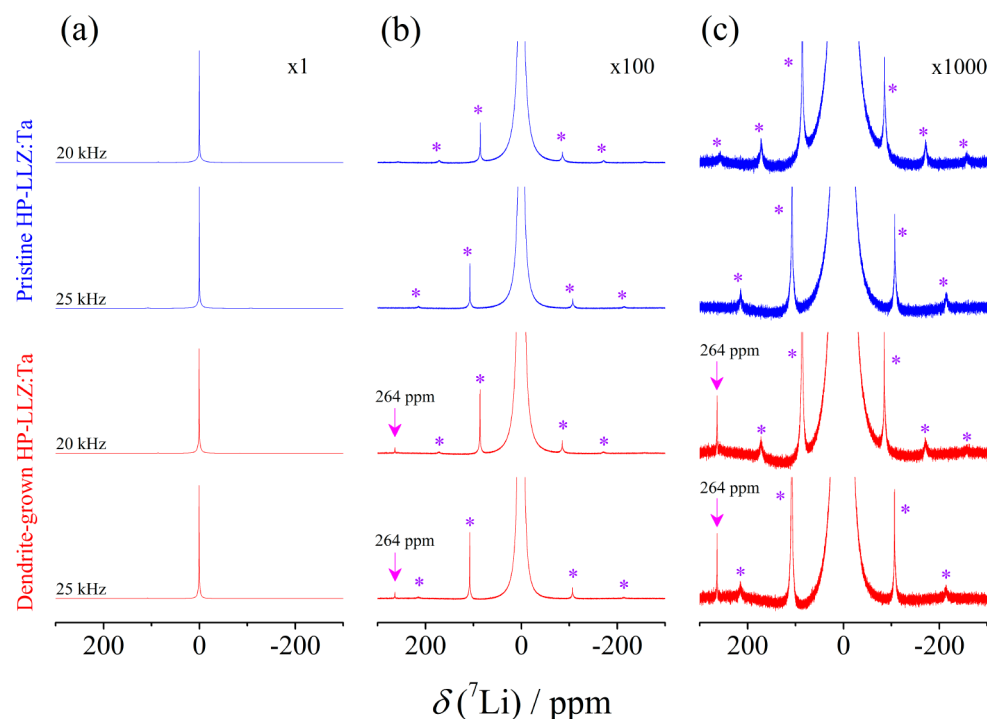
Figure 4. ^{7}Li MAS NMR spectra of pristine and dendrite-containing HP-LLZ:Ta amplified (a) 1, (b) 100, and (c) 1000 times. The signal at 264 ppm represents the existence of metallic Li. The stars (*) indicate spinning side bands.

EELS (Figure 3a). In some cases, a mixture of Li_2CO_3, Li_3N, and LiO_x was found in the grain boundaries and confirmed by EELS with an observation of Li, C, N, and O K-edges, Figure 3b. The formation of Li_3N could be explained by the reaction between metallic Li and air when transferring the specimen from the ion milling machine to the HR-TEM. Since the precursor powders for preparing HP-LLZ:Ta were either metal oxides or hydroxide, high-temperature calcination steps in Ar atmosphere make it impossible to turn the precursor powders from oxide or hydroxide into nitride. Therefore, the detection of Li_3N also suggests that the metallic Li was formed in the grain boundaries after the short circuit formation.

To further confirm that the short circuit formation inside HP-LLZ:Ta samples was due to Li dendrite, ^{7}Li MAS NMR studies were carried out to identify metallic Li inside the samples. A total of 1024 transients were collected for both the dendrite grown and pristine HP-LLZ:Ta samples at spinning frequencies of 20 and 25 kHz. All the spectra show a very strong ^{7}Li signal located at a chemical shift of 0.6 ppm, which represents Li$^+$ in HP-LLZ:Ta, (Figure 4a), along with its spinning side-bands (Figure 4b,c). In the 1000 times amplified spectra, a ^{7}Li signal was observed at 264 ppm for the dendrite-containing sample but not for the pristine one (Figure 4c). This high positive shift for ^{7}Li is a Knight shift showing the presence of metallic Li, which in turn proves that Li dendrite is the reason for the short circuit formation in HP-LLZ:Ta.[27,28] A quantitative ^{7}Li NMR analysis of Li metal has to take into account the "skin-depth" problem. This expresses the extent that the radio frequency irradiation is able to penetrate metallic species and to reach the NMR nuclei. We have calculated the skin depth to be 8.5 μm for observing the ^{7}Li signal at a Larmor frequency of 233.3 MHz using the expression given, e.g., in ref 28. Since the metallic Li particles in our case have smaller dimensions than the skin depth, a quantitative NMR analysis was assumed. The deconvolution and integration of the area

under the peak at 264 ppm give an intensity of 0.04 ± 0.005% of the total signal, which suggests that the amount of metallic Li inside the pellet is tiny even after 100 h of the dendrite-growing process by using high constant dc.

As the contact between solid electrolyte and metallic Li electrodes is a concern, a fine polish of the sample surfaces was carried out carefully by using SiC sandpapers from 800 to 4000 grit. Then, a thin Au layer was sputtered onto the polished surfaces of the samples to serve as buffer layers to further improve the contact between the solid electrolyte and metallic Li electrodes. The idea of using Au as a buffer layer is based on the fact that Au and Li form an alloy at room temperature.[29] Therefore, the homogeneously sputtered Au layers provide a comprehensive contact with the solid electrolyte once Li foils were attached and alloyed to the sputtered Au buffer layer. Also, it could help to redistribute the Li dissolution and deposition when a current is running through the cell. Figure 5 shows the impedance results from Li/LLZ:Ta/Li cells, both of which have a thickness of 0.65 mm and were with and without Au as buffer layers. The impedance spectra of the cell without Au buffer layers shows only a distorted semicircle with a total surface area resistance of ~3000 Ω cm^2. The semicircle can be simulated by the inset model circuit in Figure 5, for which R1 represents the ohmic resistance across the LLZ:Ta solid electrolyte and R2/CPE2 and R3/CPE3 represent the contact resistance from both sides of the electrodes, where R is an ohmic resistance and CPE is a constant phase element. Under an ideal situation, R2/CPE2 and R3/CPE3 should be identical and give only one semicircle, since both electrodes are the same. Under this situation, the system would give an average interface resistance of each electrode of ~1500 Ω cm^2. However, the surface roughness and the attachment of Li foils to the samples only allowed the samples to be very similar but not identical. The simulated result suggests that one side of the electrode had better contact, 1055 Ω cm^2, than the other
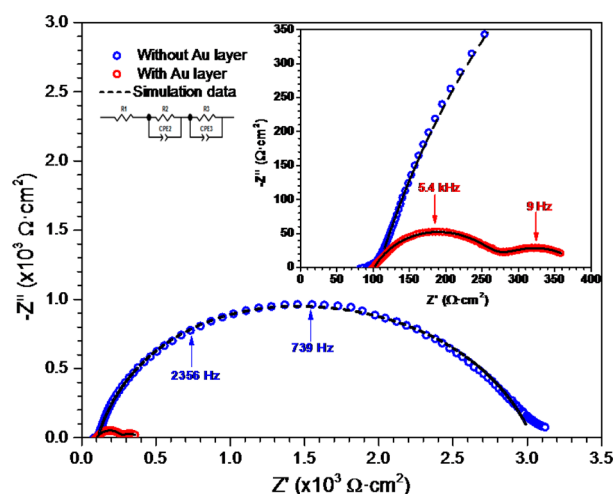
Figure 5. Impedance spectra for Li/LLZ:Ta/Li cells with and without Au buffer layers. The interface resistance can be reduced dramatically by using Au buffer layers.

Figure 6. Constant dc experiments of Li/LLZ:Ta/Li and Li/HP-LLZ:Ta/Li cells using Au buffer layers and a current density of 0.5 mA cm^{-2} at different temperatures.

side, 1871 Ω cm^2 (Table S2, SI). On the other hand, the impedance spectra of the sample with Au buffer layers consists of two semicircles and has a total resistance of only ~380 Ω cm^2, which is much lower than that for the cell without Au buffer layers. The simulation of the impedance data using the same model circuit gives a decent fit. However, the capacitances CPE2 and CPE3 are much too different, being 4.30 μF for CPE2 and 1.14 mF for CPE3, which indicates that the observed two semicircles refer to two different mechanisms (Table S2, SI). To identify the contribution of each semicircle, a detailed investigation is necessary, but that is beyond the scope of this paper. One possible explanation that combines with the impedance result from constant dc measurement (Figure S4, SI) is that the first semicircle refers to the contact between Au—Li electrode and LLZ:Ta solid electrolyte and the second semicircle could be the electrochemical reaction for Au—Li alloying.[30]

A constant dc measurement was first carried out at 50 °C for the Li/HP-LLZ:Ta/Li cell with Au buffer layers. The experiment was run for 22.5 h at a current density of 0.5 mA cm^{-2} without the formation of a short circuit (Figure 6). The thickness of Li from Li foil used during this period of time was 54.3 μm. The starting voltage was only ~22 mV, which is much lower than that for the cell without using Au buffer layers, ~0.77 V, under the same condition as shown in Figure S2 (SI) and is very close to the calculated voltage by using total ac conductivity, 11.7 mV. The much lower starting voltage is attributed to the much lower contact resistance between the Li electrodes and HP-LLZ:Ta solid electrolyte; i.e., there is much better contact when using Au buffer layers. The experiment was suspended at 8 V due to the polarization of the cell, which was a result of losing contact between the anodic electrode and HP-LLZ:Ta.

Since constant dc measurements without Au buffer layers suggest that the relative density for HP-LLZ:Ta and LLZ:Ta is not the major factor for Li dendrite formation, the same experiment was also conducted with LLZ:Ta to see if the reduction of contact resistance could relieve the Li dendrite formation by using Au buffer layers. At the same time, that the Li—Al glassy phase at the grain boundary was not reduced by metallic Li to form a short circuit can be confirmed again if the cell can reach 8 V in the experiment. Experiments were carried
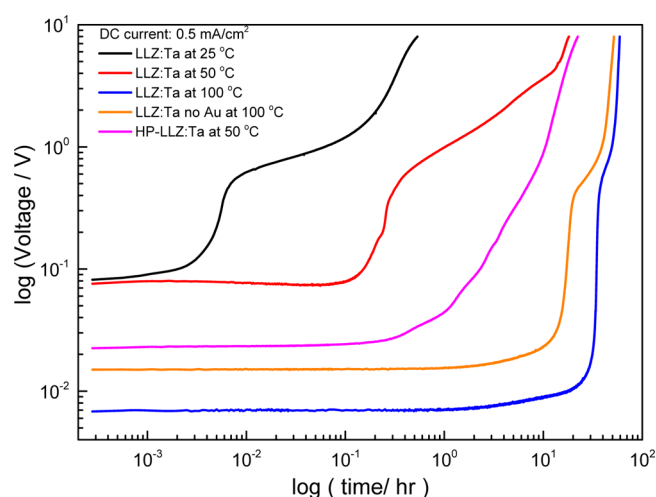
out at temperatures of 25, 50, and 100 °C. With the Au buffer layers, the experiments were free from the short circuit formation with a constant dc density of 0.5 mA cm^{-2}. However, at 25 °C, samples usually reach 8 V within a relatively short time, which can be changed from a couple hundred to thousands of seconds (~2000 s), as shown in Figure 6. In this period of time, only 1.3 μm of Li was used, which is considered to be thin. Impedance analysis was used to understand the mechanism before and after the constant dc measurement. Before the constant dc measurement, a spectrum that contains two semicircles was observed, as shown in Figure S4, which is similar to the spectrum in Figure 5. After the constant dc measurement, the diameter of the first semicircle increased from ~33 to 4.6 × 10^4 Ω cm^2, while the solid electrolyte resistance, i.e., R1, kept at the same value. However, the first semicircle of the spectrum after constant dc measurement was not able to be modeled by one R/CPE circuit. By using two R/CPE circuits, i.e., R2/CPE2 and R3/CPE3 for the first semicircle and R4/CPE4 for the second semicircle at lower frequencies, the fitting data show that the resistance for R3 is much higher than that for R2, but they have similar capacitance, ~3.2 × 10^{-8} F (Table S3, SI). The result suggests that one side of the contact between the LLZ:Ta and Au—Li electrode was dramatically lost after the constant dc measurement, even though a pressure of 0.1 MPa was applied to the cell by a spring to keep the contact between them. It is also suggested that the R2 should be assigned as the cathode side where Li was deposited and R3 should be assigned as the anode side where Li was dissolved. On the other hand, the resistance for the second semicircle, R4, was also dramatically increased without a clear reason.

The constant dc measurement was also carried out at 50 °C by using a Li/LLZ:Ta/Li cell, which had a similar result as a HP-LLZ:Ta cell (Figure 6). The starting voltage was also dramatically decreased from 0.57 to 0.08 V when comparing the sample without Au buffer layers to the one with Au buffer layers. The cell reached 8 V after about 18 h, which correlates to the use of 44 μm of Li foil. The starting voltage for the Li/LLZ:Ta/Li cell was much higher than that of the Li/HP-LLZ:Ta/Li cell, 78 vs 22 mV, which could be attributed to the lower total conductivity and less compact microstructure of LLZ:Ta. At 100 °C, the voltage of the experiment was started

from 7 mV and reached 8 V after 59 h. From the calculation, a total thickness of 143.5 μm of Li was used at this temperature, which is close to the total thickness of the used Li foil. It was also found that the constant dc measurement can be carried out by only attaching Li foil onto LLZ:Ta, i.e., without Au buffer layers, at this temperature. As expected, the starting voltage was a little bit higher than the one using Au buffer layers at 11 mV, and 125.7 μm of Li was used by this cell before the polarization voltage reached 8 V. After the experiments, all the symmetric cells for the constant dc measurements were dissembled. The anodic electrodes were all detached from the LLZ:Ta solid electrolytes, which confirms that the high polarization of the cells was due to the loss of contact between electrode and electrolyte, as suggested by IS analysis. The short-circuit-free Li/LLZ:Ta/Li cells under a constant dc density of 0.5 mA cm^{-2} also confirmed that the Li−Al glassy phase was not the reason for the short circuit formation.

Galvanostatic cyclings with stepped current densities for Li/LLZ:Ta/Li cells coated with and without Au buffer layers were carried out at 25, 50, and 100 °C. The resulting current densities for short circuit formation at different temperatures of Li/LLZ:Ta/Li cells are shown in Figure 7. The same
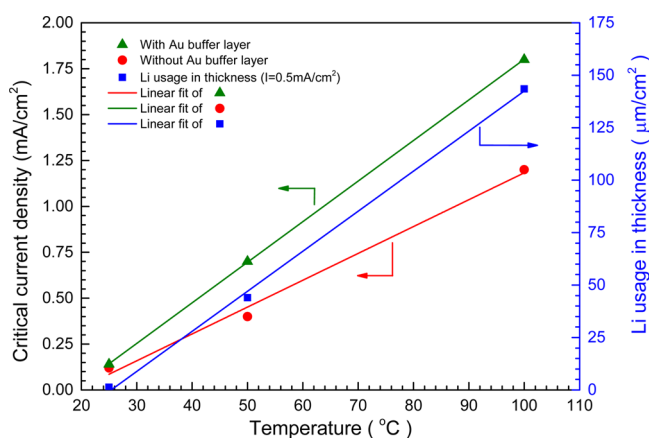

Figure 7. Temperature-dependent critical current density for Li dendrite formation and Li usage for constant dc measurements of Li/LLZ:Ta/Li cells.

experiment was also done on a Li/HP-LLZ:Ta/Li cell with Au buffer layers at 50 °C for comparison (Figure 8). At 50 °C, Li/LLZ:Ta/Li and Li/HP-LLZ:Ta/Li cells formed short circuits at current densities of 0.7 and 0.8 mA cm^{-2}, respectively, which could be considered as the same current density, even though the polarization voltage of the Li/HP-LLZ:Ta/Li cell is much lower than that of the LLZ:Ta one. The low polarization voltage also suggests that the contact between Au−Li electrodes and both LLZ:Ta and HP-LLZ:Ta solid electrolytes was still in good condition. However, the gradual increase in voltages under a current density implies an inhomogeneous dissolution and deposition of metallic Li during the cycling. When GC with a constant current density was conducted, the Li/LLZ:Ta/Li cell could be run only at a current density of 0.25 mA cm^{-2} at 50 °C without the formation of short circuit for a period of 150 h before the system was stopped manually, which could be considered as a continuously working system (Figure 9). When the current density increased to 0.3 mA cm^{-2} or higher at 50 °C, a short circuit would be formed after some cycles. A similar phenomenon was also observed at 25 °C, for which only 80

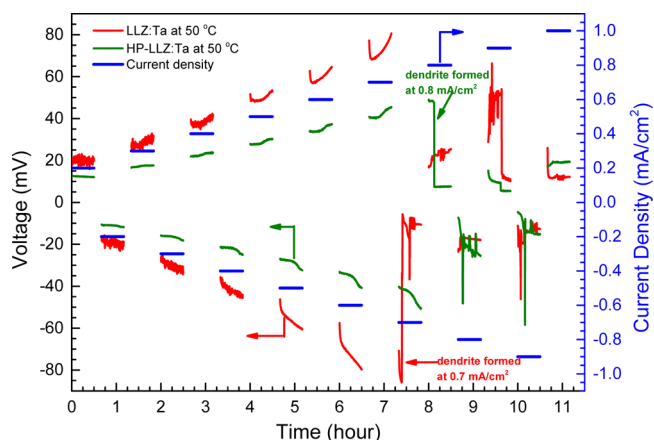**Figure 8.** Stepped current density GC for Li/LLZ:Ta/Li and Li/HP-LLZ:Ta/Li cells at 50 °C. The step width for changing current density is 100 μA cm^{-2}. Au buffer layers were used in both cells.
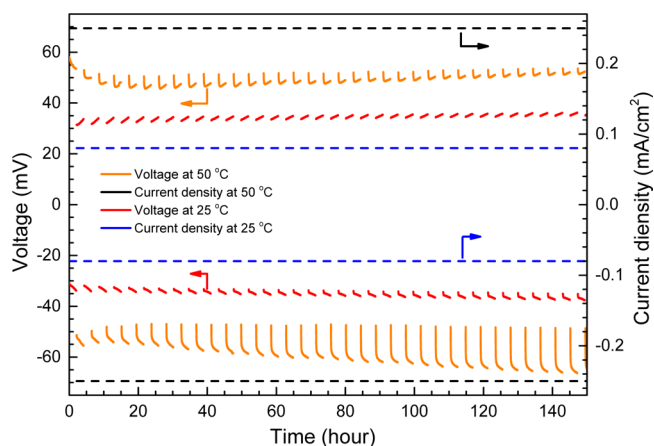

Figure 9. Constant current GC of the Li/LLZ:Ta/Li cell using Au buffer layers with 150 h of cycling at a current density of 250 μA cm^{-2} at 50 °C and 80 μA cm^{-2} at 25 °C.

μA cm^{-2} could be cycled (Figure 9). The lower tolerance current density in constant current GC than the one determined by stepped current density GC could be attributed to the repeating dissolution and deposition of metallic Li. The dissolution and deposition of Li at a higher current density caused inhomogeneous contact, which favored dendrite formation. Therefore, the current density reported for Li dendrite formation from stepped current density GC would also depend on the starting current density and how many steps are taken before Li dendrite is formed.

It is interesting to note that the loss of contact between the Au−Li electrode and LLZ:Ta electrolyte has a temperature dependency but not relative to the thickness of the Li electrodes used, i.e., similar thicknesses of Li were used when the experimental temperature and current density were the same, during the constant dc experiments. Similar observation was made for the critical current density of short circuit formation at different temperatures (Figure 7). Since the used LLZ:Ta samples were from the same batch of preparation, one could assume that the microstructure of individual samples was similar. If the conductivity of LLZ:Ta plays a major role, affecting the performance, regardless of bulk or grain boundary conductivity, an exponential dependency of performance to temperature should be expected instead of a linear dependency.

Moreover, the current density for constant current GC is much lower than what stepped current density GC measurement suggested. These observations imply that either the Au−Li alloying speed or the toughness of the Li foil may play an important role when using metallic Li and Au buffer layers as electrodes in the experiment. In considering the conventional Li ion batteries, which usually have a capacity density between 3 and 5 mA h cm^{-2}, equivalent to a usage of 14.5 and 24.2 μm of metallic Li being needed for a Li battery, the usage of the Li foil before the delamination from solid electrolyte at room temperature or below is apparently much lower than what it is needed under the current density of 0.5 mA cm^{-2}, at a C rate from $^1/_6$ to $^1/_{10}$ C. On the other hand, the use of Au buffer layers could effectively lower the contact resistance between Li electrodes and LLZ:Ta solid electrolyte, which allows for higher current density application. However, the critical current density for dendrite formation was only highly improved at high temperatures but not much at 25 °C, which may be associated with the alloying speed between Au and Li. These results lend themselves to look for even more suitable materials for further improving the contact resistance between LLZ and metallic Li. Furthermore, a homogeneous dissolution and deposition of Li at higher current density through microstructure engineering is also necessary when a practical all solid-state Li battery is going to be constructed.

CONCLUSION

Since the short circuit formation of LLZ under a constant current density of 0.5 mA cm^{-2} was a concern, high relative density LLZ:Ta and HP-LLZ:Ta were fabricated by a free sintering process and hot pressing, respectively, to answer the arising questions as addressed in the Introduction. It is proved that the short circuit formation when running a constant current density of 0.5 mA cm^{-2} through the sintered LLZ:Ta pellets was neither due to their relative density nor the reduction of Al−Li glassy phase along the grain boundaries. By using HR-TEM and EELS, Li metal and a mixture of Li$_3$N, Li$_2$CO$_3$, and LiO$_x$ phases were found along the grain boundaries, which suggests that metallic Li was present in the HP-LLZ:Ta sample after the short circuit was formed. The formation of Li dendrite was also confirmed by MAS NMR. The deconvolution of the NMR spectra gave an intensity of 0.04% of the total Li signal for metallic Li, which suggests the amount of metallic Li inside the pellet is tiny but already high enough to cause problem when making a battery.

Another concern is the high interface resistance between Li electrodes and LLZ solid electrolyte. Efforts were conducted to provide better contact by finely polishing the surfaces of LLZ:Ta and introducing Au buffer layers. The interface resistance was dramatically reduced, which prevents the Li dendrite growth when running the same dc through the cells due to a more homogeneous current distribution. However, the stepped current density GC suggests that the Li dendrite still can be formed at higher current density, which could be attributed to inhomogeneous deposition and dissolution of Li due to different conductivities of the grain and grain boundary. When constant current GC was conducted for a prolonged time, the tolerance of the current density is even lower than what is suggested by stepped current density GC. This is attributed to the repeated dissolution and deposition of Li, which can build up inhomogeneous contacts at high current density and favors the dendrite formation. It was also observed that the usage of Li under constant dc measurement and the

critical current density for Li dendrite formation are linearly temperature-dependent, which could relate to the Li−Au alloying speed or the toughness of metallic Li. At room temperature or lower, the utilization of Li and the critical current density are still too low when comparing to conventional Li ion batteries. Nevertheless, it was found that the contact between Li electrodes and LLZ electrolyte is critical for the Li dendrite formation. The resolution of the dendrite problem for higher current density or reducing interface resistance by a proper microstructure engineering to provide good contact and eliminate the difference of conductivities for the grain and grain boundary should be considered for future development of all solid-state Li batteries.

ASSOCIATED CONTENT

$\mathbf{S}$ Supporting Information

The Supporting Information is available free of charge on the ACS Publications website at DOI: 10.1021/acsami.6b00831.

> Additional details including ICP-OES element analysis, EIS fitting parameters and results, XRD patterns, TEM image, and EELS (PDF)

AUTHOR INFORMATION

Corresponding Author

*Tel: +49 2461 61 9704. Fax: +49 2461 61 2455. E-mail: c. tsai@fz-juelich.de.

Notes

The authors declare no competing financial interest.

REFERENCES

(1) Monroe, C.; Newman, J. The Impact of Elastic Deformation on Deposition Kinetics at Lithium/Polymer Interfaces. *J. Electrochem. Soc.* **2005**, *152*, A396−A404.

(2) Brissot, C.; Rosso, M.; Chazalviel, J.-N.; Lascaud, S. Dendritic Growth Mechanisms in Lithium/Polymer Cells. *J. Power Sources* **1999**, *81−82*, 925−929.

(3) Murugan, R.; Thangadurai, V.; Weppner, W. Fast Lithium Ion Conduction in Garnet-Type Li$_7$La$_3$Zr$_2$O$_{12}$. *Angew. Chem., Int. Ed.* **2007**, *46*, 7778−7781.

(4) Wolfenstine, J.; Allen, J. L.; Read, J.; Sakamoto, J. Chemical Stability of Cubic Li$_7$La$_3$Zr$_2$O$_{12}$ with Molten Lithium at Elevated Temperature. *J. Mater. Sci.* **2013**, *48*, 5846−5851.

(5) Buschmann, H.; Dölle, J.; Berendts, S.; Kuhn, A.; Bottke, P.; Wilkening, M.; Heitjans, P.; Senyshyn, A.; Ehrenberg, H.; Lotnyk, A.;

Duppel, V.; Kienle, L.; Janek, J. Structure and Dynamics of the Fast Lithium Ion Conductor "$Li_7La_3Zr_2O_{12}$. *Phys. Chem. Chem. Phys.* **2011**, *13*, 19378−19392.

(6) Ni, J. E.; Case, E. D.; Sakamoto, J. S.; Rangasamy, E.; Wolfenstine, J. B. Room Temperature Elastic Moduli and Vickers Hardness of Hot-Pressed LLZO Cubic Garnet. *J. Mater. Sci.* **2012**, *47*, 7978−7985.

(7) Ishiguro, K.; Nakata, Y.; Matsui, M.; Uechi, I.; Takeda, Y.; Yamamoto, O.; Imanishi, N. Stability of Nb-Doped Cubic $Li_7La_3Zr_2O_{12}$ with Lithium Metal. *J. Electrochem. Soc.* **2013**, *160*, A1690−A1693.

(8) Ishiguro, K.; Nemori, H.; Sunahiro, S.; Nakata, Y.; Sudo, R.; Matsui, M.; Takeda, Y.; Yamamoto, O.; Imanishi, N. Ta-Doped $Li_7La_3Zr_2O_{12}$ for Water-Stable Lithium Electrode of Lithium-air Batteries. *J. Electrochem. Soc.* **2014**, *161*, A668−A674.

(9) Sudo, R.; Nakata, Y.; Ishiguro, K.; Matsui, M.; Hirano, A.; Takeda, Y.; Yamamoto, O.; Imanishi, N. Interface Behavior between Garnet-Type Lithium-Conducting Solid Electrolyte and Lithium Metal. *Solid State Ionics* **2014**, *262*, 151−154.

(10) Suzuki, Y.; Kami, K.; Watanabe, K.; Watanabe, A.; Saito, N.; Ohnishi, T.; Takada, K.; Sudo, R.; Imanishi, N. Transparent Cubic Garnet-Type Solid Electrolyte of Al_2O_3-Doped $Li_7La_3Zr_2O_{12}$. *Solid State Ionics* **2015**, *278*, 172−176.

(11) Cheng, L.; Chen, W.; Kunz, M.; Persson, K.; Tamura, N.; Chen, G.; Doeff, M. Effect of Surface Microstructure on Electrochemical Performance of Garnet Solid Electrolytes. *ACS Appl. Mater. Interfaces* **2015**, *7*, 2073−2081.

(12) Tenhaeff, W.; Rangasamy, E.; Wang, Y.; Sokolov, A. P.; Wolfenstine, J.; Sakamoto, J.; Dudney, N. J. Resolving the Grain Boundary and Lattice Impedance of Hot-Pressed $Li_7La_3Zr_2O_{12}$ Garnet Electrolytes. *ChemElectroChem* **2014**, *1*, 375−378.

(13) Haile, S. M.; Staneff, G.; Ryu, K. H. Non-Stoichiometry, Grain Boundary Transport and Chemical Stability of Proton Conducting Perovskites. *J. Mater. Sci.* **2001**, *36*, 1149−1160.

(14) Eichinger, G. Decomposition Mechanisms of Some Lithium Ionic Conductors. *Solid State Ionics* **1981**, *2*, 289−295.

(15) Tsai, C.-L.; Dashjav, E.; Hammer, E.-M.; Finsterbusch, M.; Tietz, F.; Uhlenbruck, S.; Buchkremer, H. P. High Conductivity of Mixed Phase Al-Substituted $Li_7La_3Zr_2O_{12}$. *J. Electroceram.* **2015**, *35*, 25−32.

(16) Awaka, J.; Takashima, A.; Kataoka, K.; Kijima, N.; Idemoto, Y.; Akimoto, J. Crystal Structure of Fast Lithium-Ion-Conducting Cubic $Li_7La_3Zr_2O_{12}$. *Chem. Lett.* **2011**, *40*, 60−62.

(17) Kotobuki, M.; Kanamura, K.; Sato, Y.; Yoshida, T. Fabrication of All-Solid-State Lithium Battery with Lithium Metal Anode Using Al_2O_3-added $Li_7La_3Zr_2O_{12}$ Solid Electrolyte. *J. Power Sources* **2011**, *196*, 7750−7754.

(18) Kim, K. H.; Hirayama, T.; Fisher, C. A. J.; Yamamoto, K.; Sato, T.; Tanabe, K.; Kumazaki, S.; Iriyama, Y.; Ogumi, Z. Characterization of Grain-Boundary Phases in $Li_7La_3Zr_2O_{12}$ Solid Electrolytes. *Mater. Charact.* **2014**, *91*, 101−106.

(19) Allen, J. L.; Wolfenstine, J.; Rangasamy, E.; Sakamoto, J. Effect of Substitution (Ta, Al, Ga) on the Conductivity of $Li_7La_3Zr_2O_{12}$. *J. Power Sources* **2012**, *206*, 315−319.

(20) Wang, Y.; Lai, W. High Ionic Conductivity Lithium Garnet Oxides of $Li_{7-x}La_3Zr_{2-x}Ta_xO_{12}$ Compositions. *Electrochem. Solid-State Lett.* **2012**, *15*, A68−A71.

(21) Buschmann, H.; Berendts, S.; Mogwitz, B.; Janek, J. Lithium Metal Electrode Kinetics and Ionic Conductivity of the Solid Lithium Ion Conductors $Li_7La_3Zr_2O_{12}$ and $Li_{7-x}La_3Zr_{2-x}Ta_xO_{12}$ with Garnet-Type Structure. *J. Power Sources* **2012**, *206*, 236−244.

(22) Cao, Y.; Li, Y.-Q.; Guo, X.-X. Densification and Lithium Ion Conductivity of Garnet-Type $Li_{7-x}La_3Zr_{2-x}Ta_xO_{12}$ (x = 0.25) Solid Electrolytes. *Chin. Phys. B* **2013**, *22*, 078201−078205.

(23) Liu, K.; Wang, C.-A. Garnet-Type $Li_{6.4}La_3Zr_{1.4}Ta_{0.6}O_{12}$ Thin Sheet: Fabrication and Application in Lithium−Hydrogen Peroxide Semi-Fuel Cell. *Electrochem. Commun.* **2014**, *48*, 147−150.

(24) Huang, M.; Shoji, M.; Shen, Y.; Nan, C.-W.; Munakata, H.; Kanamura, K. Preparation and Electrochemical Properties of Zr-Site Substituted $Li_7La_3(Zr_{2-x}M_x)O_{12}$ (M = Ta, Nb) Solid Electrolytes. *J. Power Sources* **2014**, *261*, 206−211.

(25) Tong, X.; Thangadurai, V.; Wachsman, E. D. Highly Conductive Li Garnets by a Multielement Doping Strategy. *Inorg. Chem.* **2015**, *54*, 3600−3607.

(26) Matsui, M.; Wada, A.; Matsuda, Y.; Yamamoto, O.; Takeda, Y.; Imanishi, N. A Novel Aqueous Lithium−Oxygen Cell Based on the Oxygen-Peroxide Redox Couple. *Chem. Commun.* **2015**, *51*, 3189−3192.

(27) Knight, W. D. Nuclear Magnetic Resonance Shift in Metals. *Phys. Rev.* **1949**, *76*, 1259−1260.

(28) Bhattacharyya, R.; Key, B.; Chen, H.; Best, A. S.; Hollenkamp, A. F.; Grey, C. P. In Situ NMR Observation of the Formation of Metallic Lithium Microstructures in Lithium Batteries. *Nat. Mater.* **2010**, *9*, 504−510.

(29) Yuan, Y.; Liu, H. K.; Maaroof, A.; Konstantinov, K.; Liu, J.; Cortie, M. Mesoporous Gold as Anode Material for Lithium-Ion Cells. *J. New Mater. Electrochem. Syst.* **2007**, *10*, 95−99.

(30) Sinclair, D. C. Characterization of Electro-materials Using AC Impedance Spectroscopy. *Bol. Soc. Esp. Cerám. Vidrio* **1995**, *34*, 55−65.